

Neutrino Signals of Core-Collapse Supernovae in Underground Detectors

Shaquann Seadrow,^{1*} Adam Burrows,¹ David Vartanyan,¹ David Radice^{1,2}
and M. Aaron Skinner³

¹*Department of Astrophysical Sciences, Princeton University, Princeton, NJ 08544*

²*Schmidt Fellow, Institute for Advanced Study, 1 Einstein Drive, Princeton, NJ 08540*

³*Livermore National Laboratory, 7000 East Ave., Livermore, CA 94550-9234*

Accepted XXX. Received YYY; in original form ZZZ

ABSTRACT

For a suite of fourteen core-collapse models during the dynamical first second after bounce, we calculate the detailed neutrino “light” curves expected in the underground neutrino observatories Super-Kamiokande, DUNE, JUNO, and IceCube. These results are given as a function of neutrino-oscillation modality (normal or inverted hierarchy) and progenitor mass (specifically, post-bounce accretion history), and illuminate the differences between the light curves for 1D (spherical) models that don’t explode with the corresponding 2D (axisymmetric) models that do. We are able to identify clear signatures of explosion (or non-explosion), the post-bounce accretion phase, and the accretion of the silicon/oxygen interface. In addition, we are able to estimate the supernova detection ranges for various physical diagnostics and the distances out to which various temporal features embedded in the light curves might be discerned. We find that the progenitor mass density profile and supernova dynamics during the dynamical explosion stage should be identifiable for a supernova throughout most of the galaxy in all the facilities studied and that detection by any one of them, but in particular more than one in concert, will speak volumes about the internal dynamics of supernovae.

Key words: neutrinos – (stars:) supernovae: general – stars: interiors

1 INTRODUCTION

Neutrinos are produced and radiated at very high rates during and immediately after the collapse of the core of a massive star ($M \geq 8 M_{\odot}$) at its terminal stages (Burrows, Klein, & Gandhi 1992; Fischer et al. 2009; Müller & Janka 2014; Nakamura et al. 2016). For seconds during its dynamical and supernova phases, the core transitions into a proto-neutron star (PNS; Burrows & Lattimer 1986), its neutrino emissions directly reflecting in real time the internal dynamics of this violent phenomenon. Theory identifies neutrinos as the drivers of explosion (Bethe & Wilson 1985) and of the evolution of the nascent PNS. As such, neutrinos are the primary diagnostics of all stages of core behavior after stellar death and before the emergence of the residual neutron star or black hole. Stamped on the associated neutrino light curves, spectra, and mix of emitted neutrino species as a function of time are the distinctive signatures of the collapse, bounce, shock breakout, accretion, explosion, and PNS cool-

ing phases, otherwise obscured from direct scrutiny by the profound opacity to photons of the overlying stellar matter (Burrows 1990; Burrows, Hayes, & Fryxell 1995; Fischer et al. 2009; Müller & Janka 2014; Mirizzi et al. 2016; Nakamura et al. 2016; Horiuchi & Kneller 2017). By the high signal rate, followed by a abrupt cessation, one can witness in the neutrino emission history the formation, if it occurs, of a black hole (Burrows 1984,1988; Sumiyoshi et al. 2006; Fischer et al. 2009). The shock breakout burst in electron neutrinos is a firm prediction of theory that must be tested (Thompson, Burrows, & Pinto 2003; Wallace, Burrows, & Dolence 2016). The rapid neutrino light-curve variations due to turbulence in the core can constrain the convective physics predicted in most multi-dimensional models (Lund et al. 2010,2012; Tamborra et al. 2013) and considered essential to the generic mechanism of explosion (Herant et al. 1992; Burrows, Hayes, & Fryxell 1995; Janka & Müller 1996).

The supernova neutrino burst has been detected only once, from the supernova SN1987A at ~ 50 kiloparsecs (kpc) in the large Magellanic Cloud (Hirata et al. 1987; Bionta

* E-mail: shaquannseadrow@gmail.com

et al 1987). However, a total of only 11 and 8 events over ~ 12.5 and ~ 5.5 seconds, respectively, were culled. While the crude basics of PNS formation and cooling were verified in broad outline (Burrows & Lattimer 1986, 1987), the signal rates in these relatively small detectors at this extragalactic distance were paltry and most of the predicted phenomena were grossly undersampled. However, with the advent of numerous large-volume/mass underground detectors for the measurement of solar and atmospheric neutrinos (Super-Kamiokande, Abe et al. 2016; IceCube, Abbasi et al. 2011, Köpke et al. 2011) and neutrino oscillation parameters (DUNE, Ankowski et al. 2016; JUNO, Lu et al. 2015), a network of highly-capable facilities is being assembled that could record many thousands of neutrino events from a galactic core-collapse supernova (CCSN) explosion (Scholberg 2012; Beck et al. 2013). Super-K (~ 32.5 kilotonnes detecting volume) may be followed by Hyper-K (Abe et al. 2011; 0.3–0.4 Megatonnes) may be able to reach out to the Andromeda galaxy (M31) at ~ 700 kiloparsecs (kpc). With such detectors, the detailed evolution of 1) the neutrino spectra of the various neutrino types (Gallo Rosso et al. 2017), 2) the breakout burst, 3) the variation in the mass accretion rate post-bounce, but prior to explosion, 4) the accretion of shell interfaces (such as that at the boundary of the silicon and oxygen shells), 5) the explosion itself, and 6) the temporal fluctuations due to turbulent convection behind the shock could all be captured, identified, and studied.

Hence, detecting such a high-signal galactic burst and its detailed scrutiny are essential to validate and fundamentally constrain the theory of CCSN that has emerged over the last fifty years. The theory of the CCSN explosion and the theory of massive star evolution to Chandrasekhar collapse (Woosley & Weaver 1995; Woosley, Heger, & Weaver 2002; Hirschi, Meynet, & Maeder 2004; Woosley & Heger 2007; Maeder & Meynet 2012; Sukhbold et al. 2016) are intimately intertwined, so the latter is tested as well if a high-event rate galactic supernova is witnessed.

In this paper, we do not explore all the various neutrino signatures of the multi-second evolution of the supernova core, nor the retrieval in detail of the multiple parameters and inputs to CCSN theory. This would be too large a task, though aspects of this will be relegated to future installments in our series on core-collapse signatures and diagnostics¹. Rather, using recently generated two-dimensional (2D) and one-dimensional (1D) multi-group radiation/hydrodynamic models employing the code FORNAX (Burrows et al. 2018; Radice et al. 2017, Skinner et al. 2016; Wallace et al. 2016; Vartanyan et al. 2018; Skinner et al. 2018), we focus on the general overarching features of the neutrino light curve in Super-K, DUNE, JUNO, and IceCube during approximately the first second after bounce as a function of progenitor mass and between exploding and non-exploding models. The first second is the most dynamical phase. We also explore the potential identification of features in the accreted density structure, such as the silicon/oxygen interface, and estimate the effects of neutrino oscillations on the detected signals (Mirizzi et al. 2016; Scholberg 2017). We

use the 9, 10, 11, 16, 17, 19, and 21 M_{\odot} progenitor models of Sukhbold et al. (2016), as evolved in Radice et al. (2017), Burrows et al. (2018), and Vartanyan et al. (2018), for our representative progenitor model suite. The 2D variants of these models explode (Vartanyan et al. 2018; Burrows et al. 2018; Radice et al. 2017), while the spherically-symmetric 1D models do not. We use this difference to gauge the difference between exploding and non-exploding models and find that after explosion the neutrino event rate is diagnostically very different between them. Also, we can identify in many of the non-exploding models a clear signature of the accretion of the silicon/oxygen interface. Moreover, we see other characteristic timescales that can readily be discerned, as well as clear differences in all detectors between event-rate models in the various detectors for non-oscillation, normal-hierarchy, and inverted-hierarchy realizations.

In section 2, we summarize our method of calculating a neutrino light curve in the typical detector. We include in §3 a short discussion on incorporating adiabatic neutrino oscillations. We follow this in section 4 with descriptions of the various underground neutrino detectors highlighted in this paper. Then, in section 5, we summarized the salient features of FORNAX and of the 2D and 1D multi-group radiation/hydro models generated using it, and follow in section 6 with our results for the various neutrino light curves in Super-K, DUNE, JUNO, and IceCube. Sections 6.2 and 6.3 contains a general discussion of the implications of our results and section 7 summarizes our conclusions. We postpone to another paper the investigation of the extraction of the neutrino energy spectrum and of the species mix of the neutrinos emitted.

2 SIGNAL CALCULATION METHOD

In this paper, we explore the characteristic neutrino signatures in various representative underground neutrino detectors during the first crucial and dynamical second after core bounce of the supernova phenomenon. We investigate their dependence upon progenitor mass, distance, oscillation modality, and detector capabilities. The core-collapse models (§5) were generated by our FORNAX code (Skinner et al. 2016; Radice et al. 2017; Burrows et al. 2018; Vartanyan et al. 2018) and we employ the SNOwGLoBES software package (Hubber et al. 2010; Beck et al. 2013; Scholberg 2017) for computing the detected event rates in the chosen constellation of underground detectors. We have produced a pipeline that allows us easily to change the neutrino source, distance, and detector.

The neutrino energy spectra are calculated at 10,000 km from the center of each progenitor for models using either the LS220 EOS (equation of state) or the SFHO EOS. Since our focus is on the general signal characteristics of exploding vis à vis non-exploding models (§5), where all the 2D (axisymmetric) models we show explode and all the corresponding 1D (spherical) models do not, the specific EOS employed for each model is of secondary concern. We lump together the ν_{μ} , $\bar{\nu}_{\mu}$, ν_{τ} , and $\bar{\nu}_{\tau}$ neutrinos into “ ν_x ” a neutrino bin, and distinguish the electron-type (ν_e) and anti-electron-type ($\bar{\nu}_e$) species. All three species have distinct spectra and temporal evolutions. SNOwGLoBES accounts for the multitude of interactions and channels in each detector caused by

¹ Currently, in this series are Wallace et al. (2016) on the neutrino breakout burst and Morozova et al. (2018) on the gravitational wave emissions and characteristics.

each species. In an intermediate step required for signal determination, we convert the energy spectra, $\frac{dL_\nu(E_\nu, t)}{dE_\nu}$, into number-luminosity spectra:

$$\frac{d^2 N_\nu}{dE_\nu dt} = \frac{dL_\nu(E_\nu, t)}{dE_\nu} \frac{1}{E_\nu}. \quad (1)$$

For a given detector, the event rate for any given channel is

$$\frac{dN_{det}}{dt} = N_{tar} \frac{1}{4\pi D^2} \int \frac{d^2 N_\nu}{dE_\nu dt} \sigma(E_\nu) \epsilon(E) dE_\nu, \quad (2)$$

where N is the number of detected events, N_ν is (as above) the number of emitted neutrinos, the distance to the supernova is D , the number of target atoms in a given detector is N_{tar} , and the neutrino-energy-dependent cross section for a given interaction channel is $\sigma(E_\nu)$. The efficacy of neutrino detection also depends upon the efficiency of the detectors, $\epsilon(E)$, where E is the energy of the final-state product (such as an electron). This is approximately 1.0 above some detector-dependent threshold and 0.0 below it. In water Cherenkov detectors such as Super-K this threshold is ~ 5 MeV. Given the detectors we have chosen to highlight, we focus on neutrino interactions in water, ice, scintillator, and liquid argon. SNOwGLoBES imposes a particular energy binning. As a result, our model spectra, which are grouped into 20 logarithmically-spaced energy bins from 1 MeV to either 300 (for ν_{es}) or 100 MeV (for $\bar{\nu}_{es}$ and ν_{xs}) (Radice et al. 2017), must be mapped onto its grid. We do this using a straightforward interpolant, which executes one-dimensional monotonic cubic splines, across SNOwGLoBES's energy range from 0.5 to 100 MeV.

When estimating the statistical errors in the time bins selected when binning the signals (and these bin widths can be arbitrary), we multiply the height (signal rate) by the bin width, Δt , take the square root, and then divide by the bin width. Thus, we calculate the event rate error (σ) for each bin using the simple formula:

$$\sigma \Delta t = \sqrt{\frac{dN_{det}}{dt}} \Delta t. \quad (3)$$

In this way, we obtain a measure of the error in the signal rate for the given bin width. This, of course, is a function of distance. If we choose a wide bin width, the error in the average signal rate around that time bin is perforce lower, but the temporal resolution would be correspondingly diminished. As long as the detectors have good time tagging, this procedure is, of course, arbitrary and to taste. We explore some of the general conclusions using this approach in §6.3.

3 NEUTRINO OSCILLATIONS

The incoming neutrinos, by their nature, undergo neutrino oscillations. To incorporate such oscillations, we employ the approximate approach of Dighe & Smirnov (2000) to account for the adiabatic Mikheyev-Smirnov-Wolfenstein effect in the stellar envelope. We ignore possible matter oscillation effects in the Earth. The resulting mappings are:

$$F_{\nu_e} = p F_{\nu_e}^0 + (1-p) F_{\nu_x}^0, \quad F_{\bar{\nu}_e} = \bar{p} F_{\bar{\nu}_e}^0 + (1-\bar{p}) F_{\nu_x}^0,$$

and

$$4F_{\nu_x} = (1-p) F_{\nu_e}^0 + (1-\bar{p}) F_{\bar{\nu}_e}^0 + (2+p+\bar{p}) F_{\nu_x}^0. \quad (4)$$

In these equations, the initial flux of a neutrino species is F^0 and the survival probabilities are p and \bar{p} . Dighe & Smirnov (2000) also assume that the total flux of the heavy lepton species satisfies:

$$4F_{\nu_x} = F_{\nu_\mu} + F_{\nu_\tau} + F_{\bar{\nu}_\mu} + F_{\bar{\nu}_\tau}. \quad (5)$$

Utilizing the survival probabilities of Kato et al. (2017) that incorporate the θ_{13} mixing angle, we have for the Normal Hierarchy (NH):

$$p = \sin^2 \theta_{13} \quad \text{and} \quad \bar{p} = \cos^2 \theta_{12} \cos^2 \theta_{13}$$

and for the Inverted Hierarchy (IH):

$$p = \sin^2 \theta_{12} \cos^2 \theta_{13} \quad \text{and} \quad \bar{p} = \sin^2 \theta_{13}.$$

Using these survival probabilities, we, thus, obtain for the Normal Hierarchy:

$$F_{\nu_e} = \sin^2 \theta_{13} F_{\nu_e}^0 + (1 - \sin^2 \theta_{13}) F_{\nu_x}^0, \quad (6)$$

$$F_{\bar{\nu}_e} = \cos^2 \theta_{12} \cos^2 \theta_{13} F_{\bar{\nu}_e}^0 + (1 - \cos^2 \theta_{12} \cos^2 \theta_{13}) F_{\nu_x}^0, \quad (7)$$

and

$$4F_{\nu_x} = (1 - \sin^2 \theta_{13}) F_{\nu_e}^0 + (1 - \cos^2 \theta_{12} \cos^2 \theta_{13}) F_{\bar{\nu}_e}^0 + (2 + \sin^2 \theta_{13} + \cos^2 \theta_{12} \cos^2 \theta_{13}) F_{\nu_x}^0 \quad (8)$$

and for the Inverted Hierarchy:

$$F_{\nu_e} = \sin^2 \theta_{12} \cos^2 \theta_{13} F_{\nu_e}^0 + (1 - \sin^2 \theta_{12} \cos^2 \theta_{13}) F_{\nu_x}^0, \quad (9)$$

$$F_{\bar{\nu}_e} = \sin^2 \theta_{13} F_{\bar{\nu}_e}^0 + (1 - \sin^2 \theta_{13}) F_{\nu_x}^0, \quad (10)$$

and

$$4F_{\nu_x} = (1 - \sin^2 \theta_{12} \cos^2 \theta_{13}) F_{\nu_e}^0 + (1 - \sin^2 \theta_{13}) F_{\bar{\nu}_e}^0 + (2 + \sin^2 \theta_{12} \cos^2 \theta_{13} + \sin^2 \theta_{13}) F_{\nu_x}^0 \quad (11)$$

When accounting for oscillations, we use the best fit mass-mixing parameters from Capozzi et al. (2017): $\sin^2(\theta_{12}) = 2.97 \times 10^{-1}$ and $\sin^2(\theta_{13}) = 2.15 \times 10^{-2}$ for both hierarchies. The high electron densities around the inner core for these models allows us to ignore self-refraction effects on the emergent neutrino spectra, and, as implied, we ignore any possible non-adiabatic oscillation effects due to shocks and at steep compositional interfaces.

We see from equations (6) through (10) and the values of the oscillation angles that for the normal hierarchy ν_{es} in a detector come mostly from ν_{xs} at the source and $\bar{\nu}_{es}$ at the detector are a mix of ν_{xs} and $\bar{\nu}_{es}$ at the source. For the inverted hierarchy, to a slightly greater degree than for the normal hierarchy ν_{xs} source ν_{es} at the detector, while $\bar{\nu}_{es}$ in a detector were once ν_{xs} (even more so than for the normal hierarchy). These mappings are relevant for the differences in the event rates for the various detectors (differentially sensitive as they are to the various neutrino flavors) and hierarchies.

4 UNDERGROUND DETECTOR CHARACTERISTICS

4.1 Super-Kamiokande

Super-Kamiokande (Super-K; SK) is a ~ 50 -ktonne water Cherenkov neutrino detector in the Kamioka Mines in Japan, arrayed with photomultiplier tubes (*PMTs*), configured with a burst monitor for supernova neutrino bursts, and utilizing efficient false trigger rejection. It has a fiducial mass/“volume” of 32.5 ktonnes of ultra-pure water (Abe et al. 2016) and is, therefore, proton-rich. As such, it is most sensitive (Beck et al. 2013) to electron antineutrinos ($\bar{\nu}_e$) via super-allowed charged-current (CC) inverse beta decay (IBD) reaction:

$$\bar{\nu}_e + p \rightarrow e^+ + n, \quad (12)$$

which also boasts a low neutrino energy threshold of 1.8 MeV. Electron neutrinos and antineutrinos also interact via the charged-current absorption processes on Oxygen:

$$\nu_e + {}^{16}\text{O} \rightarrow e^- + {}^{16}\text{F} \quad (13)$$

and

$$\bar{\nu}_e + {}^{16}\text{O} \rightarrow e^+ + {}^{16}\text{N}. \quad (14)$$

The final state of CC interactions can also include neutrons and deexcitation gammas, and these are detectable. Detection of these secondaries can in principle be used to identify the interaction channel. Figure 1 depicts the suite of relevant cross sections for the detectors highlighted in this study, and, as indicated in the leftmost panel, that for the IBD dwarfs those for the CC interactions on oxygen. All neutrino species interact via the neutral current (NC), and, thus, contribute to the signal via the measurement of a deexcitation gamma that accompanies the neutral-current excitation of resident nuclei in reactions such as:

$$\nu_i + {}^{16}\text{O} \rightarrow \nu_i + {}^{16}\text{O}^*. \quad (15)$$

All neutrino species scatter off electrons via the process:

$$\nu_i + e^- \rightarrow \nu_i + e^-, \quad (16)$$

but this process is subdominant. However, in this Compton-like process, the directionality of the incident neutrino is partially preserved, and this fact allows neutrino-electron scattering to be the dominant means, using neutrinos alone, to determine the direction of the supernova. As seen in Figure 1, the $\nu_e - e^-$ scattering cross section exceeds that for $\bar{\nu}_e - e^-$ scattering, and these are followed by those for $\nu_x - e^-$ scattering. In order to enhance its sensitivity to the IBD reaction and the associated secondary neutron, Super-K (and its follow-on Hyper-K, at ~ 500 ktonnes) might in the future be spiked with gadolinium (Beacom & Vagins 2004; Laha & Beacom 2014).

4.2 IceCube

IceCube is currently the largest neutrino observatory, with an effective mass of ~ 3.5 Mtonnes of pure water ice (Abbasi et al. 2011). Thus comprised of water, the suite of relevant neutrino-matter interactions is the same as in water Cherenkov detectors such as Super-K (§4.1). However, given its high energy threshold (above ~ 100 MeV), it is not currently capable of identifying individual supernova neutrino

interactions, nor the energies of final-state electrons, gammas, or neutrons. Rather, the interaction of supernova neutrinos, predominantly by the IBD, will register in IceCube as a sudden increase in the background noise count rate. There are 5160 modules, each of which would detect the neutrino (mostly $\bar{\nu}_e s$ via the IBD) by the measurement in the phototubes of each module of the Cherenkov photons created by the neutrino’s charged secondaries. The Cherenkov photon yield is $\sim 178\varepsilon_e$, where ε_e is the energy of the secondary positron or electron in MeV. This yields an effective volume per detector for the measurement of a single photon (on average and to compete with the noise in the module) of ~ 590 cubic meters at $\varepsilon_e \sim 20$ MeV (Köpke et al. 2011). Multiplying this number by 5160 yields an equivalent detector mass of ~ 2.8 Mtonnes. Since the sensitivity and signal yield of a supernova in IceCube depend upon numerous detector-specific systematics, such as angular sensitivity and absorption length, a Monte Carlo analysis of the detector capabilities, best performed by the IceCube team, is necessary. Therefore, for our purposes we will assume that the effective mass for 100% detection is 3.5 Mtonnes of water ice and the reader is encouraged to scale our theoretical signal rates to any updated effective mass.

For a galactic supernova, the sharp increase in the background rate over the short few-second time period associated with a supernova neutrino burst will be unmistakable. The background rate per detector module with a 0.25-millisecond deadtime setting is estimated to be ~ 286 Hertz (Köpke et al. 2011)². It is assumed that the noise in these modules is uncorrelated and Poissonian. This yields a sigma for the collective background fluctuation of $\sim 1200\Delta t$, where Δt is the width of a time bin in seconds. This, together with the Poissonian fluctuation in the signal itself, sets the total noise floor (added in quadrature) against which to compare the average supernova signal to determine detectability. Since the Poissonian variation in the supernova signal goes as the square root of the signal, and, hence, inverse-linearly with distance, while the IceCube detector background is independent of distance, the overall noise level is dominated by the signal fluctuations at smaller distances (where the signal-to-noise will be large) and by the detector noise at large distances. This is not the case for the other detectors, for which there is effectively no background during a \sim second-long integration.

Nevertheless, IceCube, given its large effective mass, will be an excellent means to measure the neutrino- and neutrino-energy-integrated light curve. Therefore, though IceCube cannot provide event-by-event information, particle characterization, directionality, nor energy, it is still an exceptional detector for measuring the temporal development of the total neutrino flux. This can help constrain structures in the time signal such as accretion and cooling, and may provide good progenitor discrimination (see §6.2 and §6.3).

² This deadtime approach, along with the sampling rate that yielded a temporal resolution of ~ 2 milliseconds, may recently have been improved. Such changes will affect the per-module noise rate. However, for specificity and for the purposes of this study, we use the older detector characteristics as envisioned in Abbasi et al. (2011) and Köpke et al. (2011).

4.3 DUNE

The Deep Underground Neutrino Experiment (DUNE) is a ~ 40 -ktonne Liquid Argon Time Projection Chamber (LAR TPC) that is being built at the Sanford Laboratory in South Dakota’s Homestake Mine (Acciarri et al. 2016). This class of detector has high sensitivity to electron neutrinos via the charged-current reaction:

$$\nu_e + {}^{40}\text{Ar} \rightarrow e^- + {}^{40}\text{K}^*, \quad (17)$$

which has a large per-nucleus cross section (see Figure 1) and a neutrino energy threshold of only 1.5 MeV (Botella 2016). DUNE will provide the best electron-neutrino light curve, and in fact will be the only detector to provide a high-statistics ν_e signal (Ankowski et al. 2016). Electron antineutrinos also interact with Argon via the charged current reaction:

$$\bar{\nu}_e + {}^{40}\text{Ar} \rightarrow e^+ + {}^{40}\text{Cl}^*. \quad (18)$$

This interaction’s cross-section, as seen in Figure 1, is as much as two orders of magnitude smaller than that of its electron-neutrino counterpart. Of course, all species of neutrinos will contribute to the signal by elastically scattering off electrons. We do not in this study include neutral-current interactions in DUNE; there are still ongoing studies to determine the neutral-current interaction rates Argon, but these are currently unavailable in the SNOWGLoBES software (Kemp 2017; Beck et al. 2013). In a liquid argon detector, the final-state charged particles deposit kinetic energy along an ionization trail in the liquid argon. In a TPC, a voltage is applied across the liquid argon to cause charges to drift towards the anode to be collected on wire planes. The times of arrival to the wire plane allow the three-dimensional tracks to be reconstructed. Individual articles can be identified by the rate of energy loss (Ankowski et al. 2016) and, therefore, DUNE is capable of resolving the energies of the final-state charged particles, from which the incident neutrino energy can be estimated. Without a tagging mechanism, the electrons from CC interactions cannot be distinguished from the elastically-scattered electrons, but the CC interaction on Argon has such a large cross section that it dominates the signal. In summary, DUNE will provide the most accurate estimates of the electron neutrino emissions of a core-collapse supernova.

4.4 JUNO

The Jiagmen Underground Neutrino Observatory is a Liquid Scintillator Antineutrino Detector currently under construction in Southern China. This neutrino detector will utilize ~ 20 kilotons of linear alkyl-benzene hydrocarbon scintillator, and employ 17,000 high-quantum-efficiency photomultiplier tubes (Grassi 2016). Its primary research objective is to study neutrino oscillations utilizing reactor-produced electron antineutrinos. However, like water-cherenkov detectors, scintillator is proton-rich and is, therefore, sensitive to electron antineutrinos and the high-statistics IBD signal. In JUNO, scintillation light is emitted as charge particles as they lose energy in the medium, and that light is captured by PMT’s. In addition to the IBD, charge-current absorption on carbon via reactions such as:

$$\nu_e + {}^{12}\text{C} \rightarrow e^- + {}^{12}\text{N} \quad (19)$$

$$\bar{\nu}_e + {}^{12}\text{C} \rightarrow e^+ + {}^{12}\text{B}. \quad (20)$$

contribute to the signal in the detector.

The charged-current interactions for the electron and anti-electron neutrinos have thresholds of 17.34 MeV and 14.39 MeV, respectively (An et al. 2015). As indicated in Figure 1, at 20 MeV the IBD cross section is ~ 40 times larger than that for the $\bar{\nu}_e - {}^{12}\text{C}$ CC interaction. As in other detectors, all neutrino species elastically scatter off of electrons. JUNO is capable of distinguishing the IBD reaction because its final-state neutrons will quickly capture on a proton and emit a 2.2 MeV gamma ray. Pulse-shape discrimination is used to distinguish electrons from positrons, thus allowing CC absorption and electron scattering to be distinguished (Franco et al. 2011). Neutral-current interactions with carbon:

$$\nu_i + {}^{12}\text{C} \rightarrow \nu_i + {}^{12}\text{C}^*, \quad (21)$$

involving all species are possible, and these produce observable deexcitation gammas, but JUNO will have limited sensitivity to them. However, JUNO should have good event-by-event energy resolution, though directional information will be difficult to acquire in the scintillator.

5 SUPERNOVA MODELS

Between Radice et al. (2017), Burrows et al. (2018), and Vartanyan et al. (2018), we calculated a collection of supernova models starting from the 9, 10, 11, 16, 17, 19, and 21 M_\odot progenitor models of Sukhbold et al. (2016) and integrated out to ~ 1 second after core bounce. The 1D variants did not explode, while the 2D variants did. These models, while not the final word, collectively capture the wide range of detailed model expectations for the neutrino emissions and signatures that have emerged from most recent theoretical work on the supernova mechanism. The multi-group radiation/hydrodynamic code FORNAX (Skinner et al. 2018; Burrows et al. 2018) was used with twenty energy groups for each neutrino species³. The radial coordinate, r , ran from 0 to 20,000 kilometers (km) in 608 zones (both 1D and 2D), while the polar angular grid spacing (in 2D) covered the full 180° and varied smoothly in 256 zones from $\approx 0.95^\circ$ at the poles to $\approx 0.65^\circ$ at the equator. We used the LS220 (Lattimer & Swesty 1991) nuclear equation of state (EOS) for the 9, 10, and 11 M_\odot models and the SFHo nuclear equation of state (Steiner et al. 2013) for the rest, the approximate general relativistic potential formalism of Marek et al. (2006), and GR redshifts were included in the transport. The many-body correction of Horowitz et al. (2017) was incorporated into the full collection of neutrino-matter interaction rates (Burrows, Reddy, & Thompson 2006) and inelastic scattering off electrons and nucleons as described in Burrows et al. (2018) was included. In the 2D simulations, seed perturbations were include in only the 10- M_\odot model (Radice

³ For these simulations, we follow the ν_e , $\bar{\nu}_e$, and “ ν_μ ” species, where the four species, ν_μ , $\bar{\nu}_\mu$, ν_τ , and $\bar{\nu}_\tau$ are lumped together into “ ν_μ ”. For the ν_e types, the neutrino energy ε_ν varied logarithmically from 1 MeV to 300 MeV, while it varied from 1 MeV to 100 MeV for the $\bar{\nu}_{e\tau}$ and $\nu_{\mu s}$.

et al. 2017), while numerical noise was allowed to seed the turbulence in the other 2D models. The products used to determine signals in underground detectors were the associated emergent luminosity spectra for each neutrino species as a function of time.

6 RESULTS

Table 1 summarizes the total number of events at 10 kiloparsecs (kpc) expected in all detectors during the first \sim second after bounce for all models (both 1D and 2D) and for the three contexts of no-oscillation (NO), the normal hierarchy (NH), and the inverted hierarchy (IH). As expected, IceCube should experience by far the largest number of events at 10 kpc, of order 10^5 , during this time interval, though it can not distinguish interaction channel nor neutrino energy nor type. Nevertheless, the entire galaxy should be within reach for all models, whether NH or IH obtains. The total signals in the other detectors during this earlier dynamical phase are still formidable and suggest that the entire galaxy is well within reach by them. As expected, among these the more massive facilities (such as Super-K, and later Hyper-K) boast the larger event yields. At the low progenitor mass end, the 1D and 2D models yield roughly similar integrated event yields (though different light curves in detail). This is due to the earlier explosion times post-bounce of such progenitors and to their steeper density profiles. The latter translates into a more rapid decrease in the accretion rate and, hence, the accretion powered neutrino luminosity, before explosion, so that the accretion-powered phase is both weaker and shorter-lived. Diffusion from the core then starts to ascend in relative importance.

Figures 2, 3, and 4 provide the energy luminosities and RMS neutrino energies for all models (both 1D [dashed] and 2D [solid]) and neutrino species and for the no-oscillation, normal-hierarchy, and inverted-hierarchy cases. These curves depict input quantities before convolution in the various detectors, but after our oscillation model operates (if it does). The no-oscillation numbers are what the supernova models give and the NH and IH numbers reflect the result of applying the oscillation model described in §3. For higher-mass progenitors, the corresponding event yields from the 2D (exploding) models should be generally lower than those for the 1D models. In these cases, the continuation of significant accretion due to the failure in 1D to explode translates into higher neutrino luminosities for longer times. In addition, the average and root-mean-square (RMS) neutrino energies of the more massive progenitors at the later times are slightly higher than their corresponding 2D counterparts. The upshot should be significantly higher event rates for the 1D models at later times for the progenitors with shallow mass density profiles (high “compactness”; O’Connor & Ott 2011, 2013). We suggest that the distinctly different event light curves for 1D and 2D, particularly for the higher compactness models (mostly for higher progenitor mass, with exceptions), reflect in a generic sense the difference between non-exploding and exploding models. Factors of more than two in the event rates at later times (after hundreds of milliseconds) are possible. Note that one expects the temporal fluctuations in the event rates and inferred neutrino luminosities for the 2D (exploding) models to be

larger than in the 1D cases. This is a consequence of turbulence in the multi-D models (impossible in 1D) and the associated episodic nature of plume accretion onto the PNS core before, during, and just after explosion when asphericities are allowed. Fluctuations in the energy luminosities of as much as \sim 25% on timescales of \sim 10 to \sim 100 milliseconds are seen. The detection of such temporal structures could be used to constrain post-bounce and post-explosion accretion rate variations in angle and time.

6.1 Neutrino Light Curves

Figures 5, 6, 7, and 8 portray the total all-channel event rates in the Super-K, DUNE, JUNO, and IceCube detectors, respectively, for the 10 M_{\odot} and 19 M_{\odot} models, for both 1D and 2D realizations, and for all neutrino oscillation assumptions. Such plots allow one to focus on both the differences between low-mass and higher-mass light curves and on the differences as a function of neutrino hierarchy.

Since Super-K is most sensitive to $\bar{\nu}_e$ s, as Figure 5 suggests, the high signal rate in the NO (no-oscillation) case is muted in either oscillation model. For the 1D (non-exploding) case, the differences in event rate can be large, as much as \sim 40% for the low-mass progenitor and more than a factor of two for the higher-mass progenitor, but for the two 2D (exploding) models the differences between the various oscillation models in the corresponding light curves are smaller. For the exploding (2D) models, unlike in the non-exploding models (particularly for the higher progenitor mass) the largest differences between the various oscillation assumptions are at earlier post-bounce times within a few hundred milliseconds. At the later times, the NH and IH signal rates get closer. As Figure 5 suggests, during the first hundreds of milliseconds, there is generically an accretion luminosity hump that evinces a large post-bounce and post-breakout signal rate. For the low-mass progenitor this hump in 1D decays quickly (with an “e-folding” time near \sim 0.8 seconds), but for the higher-mass progenitor the 1D signal drops and then rises or flattens. For this 19- M_{\odot} progenitor, the drop is due to the accretion of the silicon/oxygen interface and the associated drop in mass flux at the shock, while the rise for the NO case and the near-flattening for the NH and IH cases are due to the fact that accretion continues in a non-exploding model and the average and RMS neutrino energies continue to grow (see Figures 2, 3, and 4) as the core contracts and the neutrinospheres compressionally heat. The neutrino-matter cross sections in detectors increase with neutrino energy (Figure 1). So, for higher-mass exploding (2D) models, the accretion of the silicon/oxygen interface results in a decrease in the event rate, but this decrease is less manifest due to the almost simultaneous explosion and reversal of net accretion. For the lower-mass progenitors, the magnitude of the density drop at this interface is smaller and explosions can occur before it, or a similar structure, is accreted (Radice et al. 2017). Hence, the accretion powered phase, the accretion of the silicon/oxygen interface itself, the progenitor-model and/or compactness (seen mostly through the overall event rate), and the explosion/no-explosion dichotomy are all in principle observables (Horiuchi et al. 2017). The NH and IH hierarchies are less easily discerned in Super-K, though the

earlier breakout burst is rather different for the two scenarios (Wallace et al. 2016).

On the other hand, DUNE (Figure 6), sensitive as it is to ν_{eS} , manifests at early post-bounce times an inversion in the event rate ordering for the NO, NH, and IH situations vis à vis Super-K for both the 10- M_{\odot} and 19- M_{\odot} . In Super-K, the early event rates around the hump are in the order NO > NH > IH for both non-exploding and exploding models, but in DUNE they are NH > IH > NO. After ~ 200 milliseconds, in both the 10- M_{\odot} and 19- M_{\odot} non-exploding models this order reverses, and is NO > IH > NH. So, for the non-exploding models and at later times, the NH/IH order reverses in DUNE relative to the behavior in Super-K. For the exploding (2D) models, the event rate differences between the hierarchies are smaller. However, we note that at the earlier times (<200 milliseconds after bounce) the light curve shapes in DUNE and Super-K are very different, reflecting their differential neutrino flavor sensitivities. This, along with a potential capacity in each detector to discriminate channel, flavor, and spectra, could be used to derive both oscillation modality and progenitor-model constraints.

As Figures 5, 7, & 8 demonstrate, due to the $\bar{\nu}_e$ sensitivity in all three, the light curves in JUNO, IceCube, and Super-K are qualitatively similar. IceCube, however, if the fiducial volume we have assumed for it obtains, would experience a much higher rate of signal accumulation⁴. Nevertheless, the temporal structure of the neutrino burst during the dynamical supernova phase is best discerned via IceCube, but the flavor and spectral character of the burst can be determined clearly only via the channel and event energy discrimination that might be possible in the collective combination of Super-K, DUNE, and JUNO. The differential sensitivity of Super-K and JUNO on the one hand and DUNE on the other vis à vis $\bar{\nu}_{eS}$ and ν_{eS} will be particularly revealing. As noted, we have focused in this paper on all-channel energy-integrated rates and defer a discussion of the spectral and channel capabilities in these three detectors (and in Hyper-K) to a later paper.

In Figures 9, 10, 11, and 12, we present all the all-channel light curves for all the progenitors studied, for both 1D (non-exploding) and 2D (exploding) realizations in Super-K, DUNE, JUNO, and IceCube. The basic systematics with progenitor articulated and described above using only the 10- M_{\odot} to 19- M_{\odot} models survives. The wide range of signal rates as a function of progenitor mass and compactness is clear. For the non-exploding models, the early-time event rates can vary by a factor of ~ 2 , while the late-time event rates can vary by a factor of ~ 10 for the non-oscillating case and ~ 5 for the oscillating cases. For the exploding models, variations of at least a factor of ~ 2 are expected from 9- M_{\odot} to 21- M_{\odot} . Since a galactic supernova will almost certainly be measured electromagnetically, the distance to the supernova will be known. Given the distance, the absolute flux and fluence can be determined and with it some measure of the core structure/compactness of the progenitor. The electromagnetic data will likely reveal the progenitor

mass, so the absolute neutrino signal can be paired with the progenitor star to constrain stellar evolution and supernova models together.

6.2 Detection Ranges and Feature Measurement

Table 1 provides the total number of events expected at 10 kiloparsecs in all the models and for all the detectors studied. For Super-K, DUNE, and JUNO the effective background count rate is negligible during times of order one second. Therefore, if we assume Poisson statistics for the signal fluctuations, deriving the total number of events to $\sim 10\%$ accuracy at 1- σ would require that $\frac{1}{\sqrt{N}} \sim 0.1$, where N is the number of events. This criterion yields $N \sim 100$, and, therefore, a range of ~ 100 kiloparsecs for these three detectors. This encompasses the entire Milky Way and the Magellanic Clouds. However, an accuracy of 10% for the entire signal during the dynamical “first second” is not that impressive. Astronomers would want to discern various temporal structures, such as the post-bounce accretion hump. Using Figures 5–7 and 9–11, we can determine that to capture the number fluence during the accretion hump (assuming that it lasts for ~ 200 milliseconds) to at least $\sim 10\%$ accuracy the distance of the supernova needs to be closer than 20 to 25 kpc for Super-K and ~ 10 to 15 kpc for DUNE, depending upon oscillation and progenitor model. This still encompasses most of the Milky Way. The corresponding numbers for JUNO are in most cases in between. In general, and approximately, in order to discern a temporal feature, “ i ”, of width Δt whose average signal rate is $\dot{E}_i (= \frac{dN_{det}}{dt})$ to within a fraction, f , requires that $f > N_i^{-1/2} \sim \frac{1}{(\dot{E}_i \Delta t)^{1/2}}$. For example, to identify a temporal fluctuation in the event rate of 10% that might occur over a Δt of 10 milliseconds requires a “background” \dot{E}_i of $\sim 10,000$ Hertz. In Super-K, the higher-mass progenitors need to be within ~ 5 –6 kpc to achieve this, depending upon oscillation model and epoch of fluctuation. Such fluctuations might arise due to episodic accretion or rotation and would usefully constrain the character of the turbulence in the core and behind the shock wave. A feature with a larger Δt would be discernible out to a correspondingly greater distance. In fact, the range out to which one could discern a fluctuation f of duration Δt is proportional to f and $\sqrt{\Delta t}$. Hence, to capture a small fluctuation of 1% over an interval of 10 milliseconds would require a supernova distance below ~ 1 kpc for most models. Only of order 1% of the galaxy is within this distance.

Nevertheless, as Figures 5–7 and 9–11 clearly demonstrate, the general evolution of the neutrino light curve during the crucial dynamical supernova phase will be accessible for a core-collapse supernova going off in most of our galaxy. Moreover, as Figures 9–11 reveal, the range of event rates as a function of progenitor can vary by a factor of two to five, depending upon whether the model explodes and, to some degree, upon whether the NH or IH obtains. The arguments just above indicate that such a spread can be discriminated in Super-K, DUNE, and JUNO for supernovae throughout the galaxy. For instance, for the normal hierarchy and non-exploding models, the 9- M_{\odot} and 10- M_{\odot} progenitor predictions can be distinguished in Super-K out to ~ 100 kpc. For the exploding models, the variation in signal rate is approximately a factor of two and the $\sim 25\%$ variation from model

⁴ At 10 kiloparsecs, a CCSN would register during the first second of post-bounce evolution $\sim 10^4$ times as many events in IceCube as were culled by Kamioka II from SN 1987A. The other detectors highlighted here would witness $\sim 10^2$ times more events.

to model seen in this model suite can be resolved out to 50–100 kpc. Of course, more precise discrimination requires closer supernovae, but the numbers for the parameter examples given are already rather impressive.

IceCube has a significant background count rate. The supernova would be identified by a rise in this background. If we assume a background of 1200 Δt Hertz (§4.2), then the signal to background ratio for the first second after collapse ranges from ~ 100 to ~ 300 at 10 kpc. This implies that a supernova anywhere in the Milky Way could be detected in IceCube. Since the Poissonian noise fluctuation of the signal itself binned in 10-millisecond bins exceeds that in the detector for distances less than ~ 3 –5 kpc, the signal in IceCube will be detector-noise-limited for much of the galaxy. At a signal rate (\dot{E}) of $\sim 10^5$ Hertz, the signal-to-background ratio is ~ 9 for $\Delta t = 10$ milliseconds and ~ 4 for $\Delta t = 2$ milliseconds. At an \dot{E} of $\sim 3 \times 10^5$, the corresponding numbers are ~ 27 and ~ 12 . Therefore, at the higher rate (see Figure 12), IceCube should be able to measure the event rate in 10-millisecond bins to $\sim 4\%$, and in 20-millisecond bins to $\sim 3\%$. This would enable exquisite model discrimination at 10 kpc. Within a given oscillation paradigm, IceCube is able to discriminate the various progenitors for any galactic CCSN solely on the basis of the general level of flux measured. Hence, with $\sim 10^2$ times the signal rate found in the other detectors, it should be able to achieve for a time bin of 10 milliseconds and distances less than ~ 5 kpc (approximately interior to which the signal noise exceeds the detector noise) ~ 10 times the precision in the estimation of instantaneous event rate (ten times smaller f_s). Hence, IceCube will be able to provide exquisite all-channel neutrino light curves throughout most of the galaxy.

In Table 2, we provide the ranges for Super-K, JUNO, and DUNE at which the signal-to-noise ratio is five for a measurement of the flux at the first post-bounce peak, centered in a 10-ms bin around that time. We do this for all models and for both the Normal and Inverted hierarchies. This procedure can be applied to any light-curve feature, and the results depicted in Table 2 are merely representative. Nevertheless, Table 2 gives the reader a quantitative estimate of the supernova ranges out to which an important light-curve feature could be discerned by an important subset of current and near-term underground neutrino observatories.

6.3 Temporal Feature Registration

If a measurement is signal Poisson-limited (as it is for Super-K, DUNE and JUNO), the precision with which a temporal feature (a hump or fluctuation) can be registered in time goes roughly as the feature width, Δt , divided by the square root of the event number, N_i , under the feature. This is the “centroiding” problem and implies that the distance out to which one can time-register a feature scales with the feature width⁵. If the feature has a width of 10 milliseconds, it will require $N_i \sim 100$ to register the feature to within ~ 1 millisecond. As Wallace et al. (2016) have shown, to determine the peak time of the ν_e breakout burst to within ~ 1

millisecond in the inverted hierarchy requires a supernova at a distance of less than ~ 4 kpc. For the normal hierarchy, the breakout burst is much less easily captured (see §3). However, for a given underlying model, the huge number of events expected during the subsequent dynamical phase would enable better fractional registration of longer duration features. For instance, using Super-K data, centroiding the accretion hump of ~ 200 millisecond duration for the exploding 19- M_\odot progenitor to within ~ 10 milliseconds could in principle be done out to a range of ~ 10 kpc. For context, the mean time between single events during the SN 1987A campaign was ~ 1 second.

We note that when a black hole forms, the neutrino signal should immediately shut off (Burrows 1984). This would be a precipitous drop, effectively an edge, and a detector’s capacity to determine the precise time of black hole formation will be limited by the instantaneous event rate just before that time. Though for this paper we did not simulate the neutrino light curve for black hole formation, the event rates provided for the 1D models in the relevant figures are indicative of the approximate rates when such a secondary collapse to a black hole would occur. Using these numbers suggests that the time of black hole formation could be determined in Super-K, DUNE, or JUNO to one millisecond out to 10–20 kpc.

7 CONCLUSIONS

Most of the neutrino burst signal diagnostic of supernova dynamics and the hydrodynamics of core-collapse occurs in this first \sim second after core bounce. However, most of the signal occurs later during the subsequent tens-of-seconds of PNS cooling and deleptonization (Burrows & Lattimer 1986). Nevertheless, the neutrino light curve, spectral evolution, and species mix during this first crucial phase uniquely bear the stamp of the internal dynamics of the supernova. In this paper, we have presented models of the all-channel neutrino light curve (event-rate/signal evolution) in four current and planned underground neutrino detectors for seven exploding and non-exploding progenitor models, with and without neutrino oscillations, in order to quantify the systematic variations of the neutrino event rate evolution with progenitor mass, oscillation model, and whether the model exploded. We identify features in the light curves diagnostic of each, as well as of the pre-collapse core mass density profile, the accretion of the silicon/oxygen interface, and temporal variations due to episodic accretion events. The network of large-volume neutrino detectors that is emerging around the world will be hugely capable of constraining, perhaps in detail, the evolution in real time of the supernova phenomenon for any galactic core-collapse supernova and providing much-needed ground truth for the theory of supernovae upon which so many have labored these last five decades⁶.

⁵ This is a very approximate statement of the more general Cramer-Rao theorem (Hogg & Craig 1978).

⁶ All of the models calculated in this paper are available upon request.

ACKNOWLEDGEMENTS

The authors acknowledge support under U.S. NSF Grant AST-1714267 and the Max-Planck/Princeton Center (MPPC) for Plasma Physics (NSF PHY-1144374). and the DOE SciDAC4 Grant DE-SC0018297 (subaward 00009650). DR acknowledges support from a Frank and Peggy Taplin Membership at the Institute for Advanced Study. In addition, this material is based upon work supported by the U.S. Department of Energy, Office of Science, Office of Advanced Scientific Computing Research, and the Scientific Discovery through Advanced Computing (SciDAC) program under Award Number DE-SC0018297 (subaward 00009650). The authors employed computational resources provided by the TIGRESS high performance computer center at Princeton University, which is jointly supported by the Princeton Institute for Computational Science and Engineering (PICSciE) and the Princeton University Office of Information Technology, and by the National Energy Research Scientific Computing Center (NERSC), which is supported by the Office of Science of the US Department of Energy (DOE) under contract DE-AC03-76SF00098. The authors express their gratitude to Ted Barnes of the DOE Office of Nuclear Physics for facilitating their use of NERSC.

REFERENCES

- Abbasi, R. et al. 2011, *A&A*, 535, A109
Abe, K. et al. 2011, arXiv:1109.3262
Abe, K. et al. 2016, *Astropart. Phys.*, 81, 39
Acciarri, R., Acero, M.A., Adamowski, M., et al. 2016, arXiv:1601.02984
An, F., An, G., An, Q., et al. 2016, *Journal of Physics Nuclear Physics G*, 43, 030401
Ankowski, A. et al., “Supernova Physics at DUNE,” in *Supernova Physics at DUNE*, Blacksburg, Virginia, USA, March 11-12, 2016, arXiv:1608.07853
Beacon, J.F. & Vagins, M.R. 2004, *Phys. Rev. Lett.*, 93, 171101
Beck, A. et al. 2013, “Snowglobes”, <http://phy.duke.edu/~schol/snowglobes/>
Bethe, H. & Wilson, J.R. 1985, *ApJ*, 295, 14
Bionta, R.M. et al. 1987, *Phys. Rev. Lett.*, 58, 1494
Burrows, A. 1984, *ApJ*, 283, 848
Burrows, A. & Lattimer, J.M. 1986, *ApJ*, 307, 178
Burrows, A. & Lattimer, J.M. 1987, *ApJ*, 318, L63
Burrows, A. 1988, *ApJ*, 334, 891
Burrows, A. 1990, *Ann. Rev. Nucl. Part. Sci.*, 40, 181
Burrows, A., Klein, D., & Gandhi, R. 1992, *Phys. Rev. D*, 45, 3361
Burrows, A., Hayes, J., & Fryxell, B.A. 1995, *ApJ*, 450, 830
Burrows, A., Reddy, S., & Thompson, T.A. 2006, *Nuclear Physics A*, 777, 356-394
Burrows, A., Vartanyan, D., Dolence, J.C., Skinner, M.A., & Radice, D. 2018, *Space Science Reviews*, 214, 33 (arXiv:1611.058959)
Capozzi, F., Valentino, F., Lisi, E., Marrone, A., Melchiorri, A., & Palazzo, A. 2017, *Phys. Rev. D*, 95, 096014
Dighe, A.S. & Smirnov, A.Y. 2000, *Phys. Rev. D*, 62, 033007
Fischer, T., Whitehouse, S.C., Mezzacappa, A., Thielemann, F.-K., Liebendörfer, M. 2009, *A&A*, 499, 1
Franco, D., Consolati, G., & Trezzi, D. 2011, *Phys. Rev. C*, 83, 015504
Grassi, M. 2016, *Proceedings for the XIII International Conference on Heavy Quarks and Leptons(HQL2016)*, 22- 27
May, 2016, Blacksburg, Virginia, USA. <http://pos.sissa.it/cgi-bin/reader/conf.cgi?confid=274>, id.73, 73
Hirata, K. et al. 1987, *Phys. Rev. Lett.*, 58, 1490
Hirschi, R., Meynet, G., & Maeder, A. 2005, *A&A*, 425, 649-670
Hogg, R.V. & Craig, A.T. 1978, *Introduction to Mathematical Statistics*, 4th Edition (Macmillan, New York)
Horiuchi, S., Nakamura, K., Takiwaki, T., & Kotake, K. 2017, arXiv:1708.08513
Horiuchi, S. & Kneller, J.P. 2017, arXiv:1709.01515
Horowitz, C.J. 2002, *Phys. Rev. D*, 65, 043001
Horowitz, C.J., Caballero, O.L., Lin, Z., O’Connor, E., & Schwenk, A. 2017, *Phys. Rev. C*, 95, 025801 (arXiv:1611.05140)
Hubber et al. 2010
Kemp, E. 2017, *Astronomische Nachrichten*, 338, 993
Janka, H.-T., & Müller, E. 1996, *A&A*, 306, 167
Kato, C., Nagakura, H., Furusawa, S., et al. 2017, *ApJ*, 848, 48
Kpke, L. et al. 2011, *Contribution to the “5th Symposium on Large TPCs for Low Energy Rare Events and Workshop on Neutrinos from Supernovae,”* Paris, Dec. 16-17, 2010, arXiv:1106.6225
Laha, R. & Beacom, J.F. 2014, *Phys. Rev. D*, 89, 063007
Lattimer, J.M., & Swesty, F. D. 1991, *Nucl. Phys.*, A535, 331
Lu, J.-S., Cao, J., Li, Y.-F., & Zhou, S. 2015, *JCAP*, 5, 0044
Lund, T., Marek, A., Lunardini, C., Janka, H.-T., & Raffelt, G. 2010, *Phys. Rev. D*, 82, 063007
Lund, T., Wongwathanarat, A., Janka, H.-T., Müller, E., & Raffelt, G. 2012, *Phys. Rev. D*, 86, 105031
Maeder, A. & Meynet, G. 2012, *Rev. Mod. Phys.*, 84, 25-63
Marek, A., Dimmelmeier, H., Janka, H.-T., Müller, E., & Buras, R. 2006, *A&A*, 445, 273
Mirizzi, A., Tamborra, I., Janka, H.-T., Saviano, N., Scholberg, K., Bollig, R., Hüdepohl, L., & Chakraborty, S. 2016, *Nuovo Cimento*, 39, 1-112 (arXiv:1508.00785)
Morozova, V., Radice, D., Burrows, A. & Vartanyan, D. 2018, submitted to *ApJ*(arXiv:1801.01914)
Müller, B., & Janka, H.-T. 2014, *ApJ*, 788, 82 (arXiv:1402.3415)
Nakamura, K., Horiuchi, S., Tanka, M., Hayama, K., Takiwaki, T., & Kotake, K. 2016, *MNRAS*, 461, 3296 (arXiv:1602.03028)
E. O’Connor, C.D. Ott, *ApJ***730**, 70 (2011)
E. O’Connor, C.D. Ott, *ApJ***762**, 126 (2013)
Radice, D., Burrows, A., Vartanyan, D., Skinner, M.A., Dolence, J.C. 2017, *ApJ*, 850, 43 (arXiv:1702.03927)
Gallo Rosso, A., Vissani, F., & Volpe, M.C. 2017, arXiv:1712.05584
Scholberg, K. 2012, *Ann. Rev. Nucl. Part. Sci.*, 62, 81
Scholberg, K. 2017, arXiv:1707.06384
Skinner, M.A., Burrows, A., & Dolence, J. 2016, *ApJ*, 831, 81 (arXiv:1512.00113)
Skinner, M.A., Dolence, J.C., Burrows, A., Radice, D. & Vartanyan, D. 2018, in preparation
Steiner, A.W., Hempel, M., & Fischer, T., *ApJ*, 774, 17 (2013).
SFHo EOS
Sukhbold, T., Ertl, T., Woosley, S.E., Brown, J.M., & Janka, H.-T. 2015, *ApJ*, 821, 38
Sumiyoshi, K., Yamada, S., Suzuki, H., & Chiba, S. 2006, *Phys. Rev. Lett.*, 97, 091101
Tamborra, I., Hanke, F., Müller, B., Janka, H.-T., & Raffelt, G. 2013, *Physical Review Letters*, 111, 121104
Thompson, T.A., Burrows, A., & Pinto, P. 2003, *ApJ*, 592, 434
Vartanyan, D., Burrows, A., Radice, D., Skinner, M.A., & Dolence, J.C. 2018, accepted to *MNRAS*(arXiv:1801.08148)
Wallace, J., Burrows, A., & Dolence, J. 2016, *ApJ*, 817, 182
Woosley, S.E., Heger, A., & Weaver, T.A. 2002, *Rev. Mod. Phys.*, 74, 1015
Woosley, S. E., & Heger, A. 2007, *Phys. Rep.*, 442, 269

Table 1. Total number of events for a given progenitor for various detectors at 10 kiloparsecs during the earlier “supernova” dynamical phase. We provide the total number of accumulated events within our calculational time near ~ 1 second, starting at 50 ms before bounce and ending near as long as ~ 950 ms after bounce. These terminal times after bounce are given in the table heading. NO stands for “no oscillation”, NH stands for “normal hierarchy”, and IH stands for “inverted hierarchy”.

	9 M_{\odot}		10 M_{\odot}		11 M_{\odot}		16 M_{\odot}		17 M_{\odot}		19 M_{\odot}		21 M_{\odot}	
	1D (778 ms)	2D (950 ms)	1D (838 ms)	2D (950 ms)	1D (887 ms)	2D (616 ms)	1D (942 ms)	2D (950 ms)	1D (944 ms)	2D (950 ms)	1D (937 ms)	2D (950 ms)	1D (928 ms)	2D (950 ms)
Super-K (NO)	1057	1143	2114	1743	2100	1163	3449	2092	3683	2278	4652	2573	3402	1971
Super-K (NH)	880	1096	1600	1591	1401	1002	2184	1716	2321	1870	2837	2112	2147	1642
Super-K (IH)	815	1076	1452	1528	1223	947	1879	1585	1996	1724	2431	1944	1844	1526
DUNE (NO)	471	476	1200	817	1244	534	2182	1011	2345	1132	3060	1275	2155	949
DUNE (NH)	485	620	897	929	711	552	1099	946	1168	1048	1413	1193	1077	910
DUNE (IH)	475	529	1083	859	1041	542	1762	987	1888	1102	2417	1247	1737	936
JUNO(NO)	852	933	1652	1423	1643	948	2662	1701	2837	1852	3550	2093	2625	1611
JUNO (NH)	715	906	1249	1311	1096	827	1672	1409	1772	1534	2136	1732	1643	1357
JUNO (IH)	661	885	1128	1255	950	779	1425	1300	1508	1414	1804	1594	1398	1259
IceCube (NO)	113854	123084	227649	187727	226195	125254	371439	225329	396647	245295	501013	277047	366332	212280
IceCube (NH)	94815	118007	172308	171384	150855	107922	235201	184820	249963	201397	305563	227457	231191	176868
IceCube (IH)	87733	115928	156345	164540	131685	102004	202312	170721	215008	185686	261827	209335	198581	164353

Table 2. Ranges (in kpc) for the determination at $5\text{-}\sigma$ of the neutrino event rate for a 10-ms bin centered on the first peak following breakout for both the Normal and Inverted hierarchies. This is usually associated with the accretion-powered phase, but for DUNE, given that the signal in it is dominated by the ν_e component at Earth, the peak times for a give model do not match those in the corresponding neutrino light curves in Super-K, JUNO, and IceCube. Times at which the bins are centered for Super-K and JUNO are given in the heading and for DUNE in the body of the Table.

	9 M_{\odot}		10 M_{\odot}		11 M_{\odot}		16 M_{\odot}		17 M_{\odot}		19 M_{\odot}		21 M_{\odot}	
	1D (109 ms)	2D (101 ms)	1D (164 ms)	2D (124 ms)	1D (131 ms)	2D (113 ms)	1D (112 ms)	2D (96 ms)	1D (118 ms)	2D (103 ms)	1D (153 ms)	2D (105 ms)	1D (76 ms)	2D (76 ms)
Super-K (NH)	9.60	9.35	10.61	10.01	10.27	9.90	11.25	10.88	11.62	11.20	12.51	11.81	10.91	10.73
Super-K (IH)	9.01	8.83	9.93	9.47	9.58	9.30	10.52	10.26	10.86	10.55	11.59	11.10	10.30	10.18
JUNO (NH)	8.70	8.48	9.59	9.09	9.30	8.98	10.19	9.88	10.53	10.16	11.26	10.71	9.89	9.74
JUNO (IH)	8.16	8.00	8.98	8.59	8.68	8.43	9.53	9.30	9.83	9.57	10.45	10.06	9.33	9.22
	(113 ms)	(112 ms)	(170 ms)	(116ms)	(134 ms)	(114 ms)	(115 ms)	(106 ms)	(120 ms)	(110 ms)	(157 ms)	(112 ms)	(79 ms)	(81 ms)
DUNE (NH)	6.89	6.69	7.85	7.23	7.43	7.11	8.20	7.90	8.51	8.15	9.28	8.628	7.88	7.75
	(153 ms)	(112 ms)	(170 ms)	(168 ms)	(134 ms)	(127 ms)	(115 ms)	(106 ms)	(120 ms)	(118 ms)	(157 ms)	(145 ms)	(79 ms)	(81 ms)
DUNE (IH)	6.65	6.36	7.83	7.03	7.25	6.88	7.86	7.50	8.22	7.81	9.46	8.50	7.18	7.10

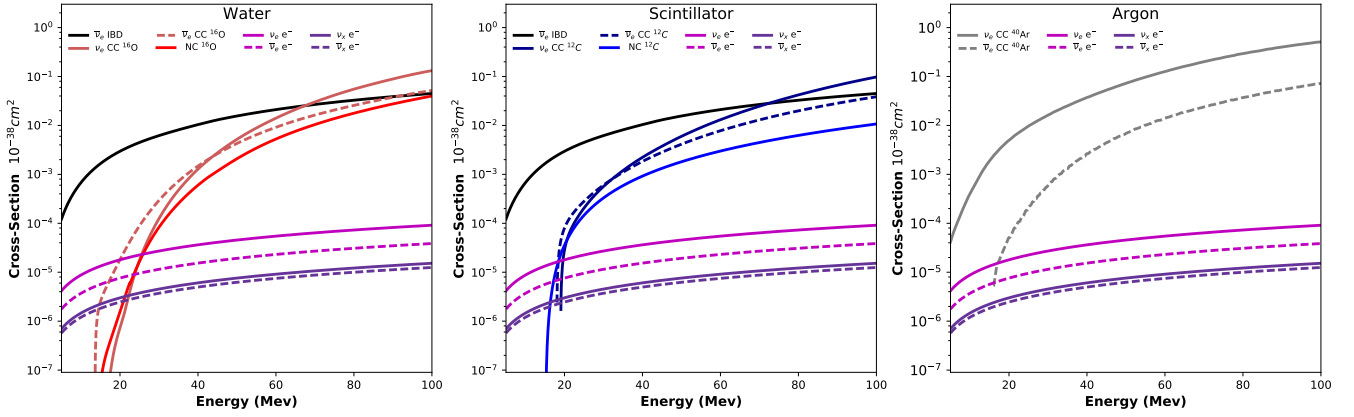


Figure 1. Above are the energy-dependent cross sections for the neutrino-matter interactions in water (left), scintillator (center), and liquid argon (right). These cross sections were provided by the SNOwGLoBES software (Beck et al 2013), and we focus on the neutrino energies up to ~ 100 MeV.

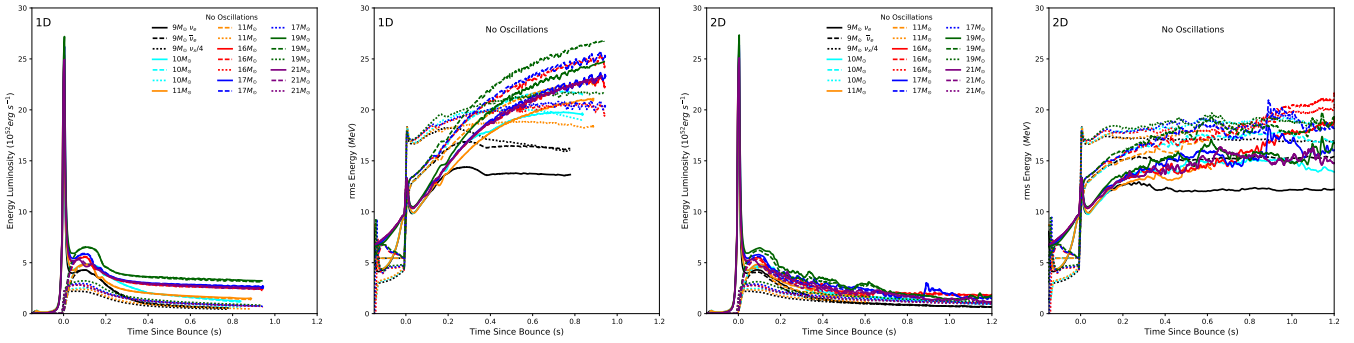


Figure 2. Energy luminosities (in units of 10^{52} ergs s^{-1}) and root-mean-square (rms) neutrino energies (in units of MeV) for all the 1D non-exploding models (left two figures) and 2D exploding models (right two figures) for the no-oscillation case. The dashed curves are the 1D models and the solid curves are the 2D models.

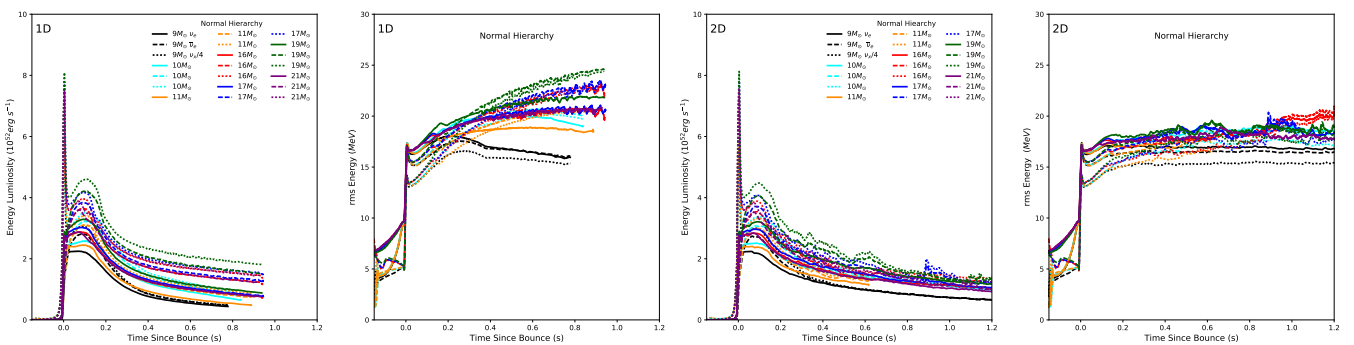


Figure 3. Energy luminosities (in units of 10^{52} ergs s^{-1}) and root-mean-square (rms) neutrino energies (in units of MeV) for all the 1D non-exploding models (left two figures) and 2D exploding models (right two figures) for the normal-hierarchy oscillation case. The dashed curves are the 1D models and the solid curves are the 2D models.

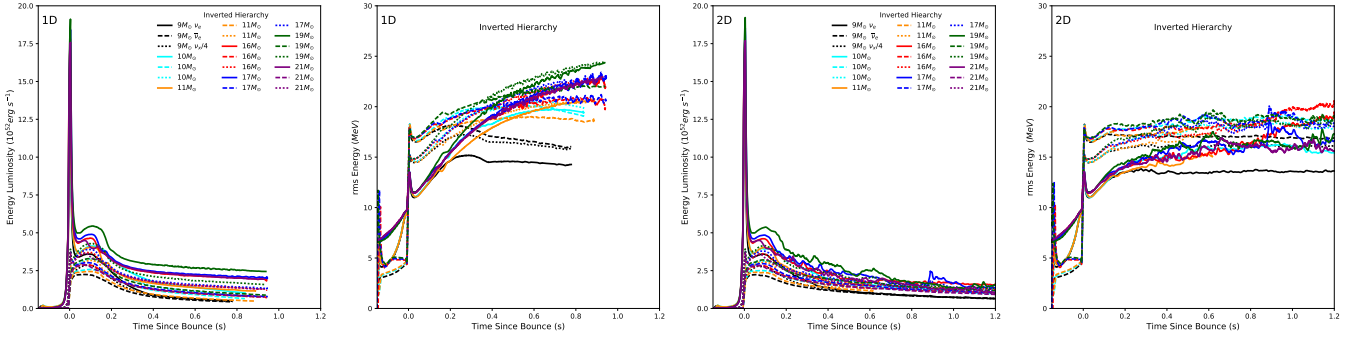


Figure 4. Energy luminosities (in units of $10^{52} \text{ erg s}^{-1}$) and root-mean-square (rms) neutrino energies (in units of MeV) for all the 1D non-exploding models (left two figures) and 2D exploding models (right two figures) for the inverted-hierarchy oscillation case. The dashed curves are the 1D models and the solid curves are the 2D models.

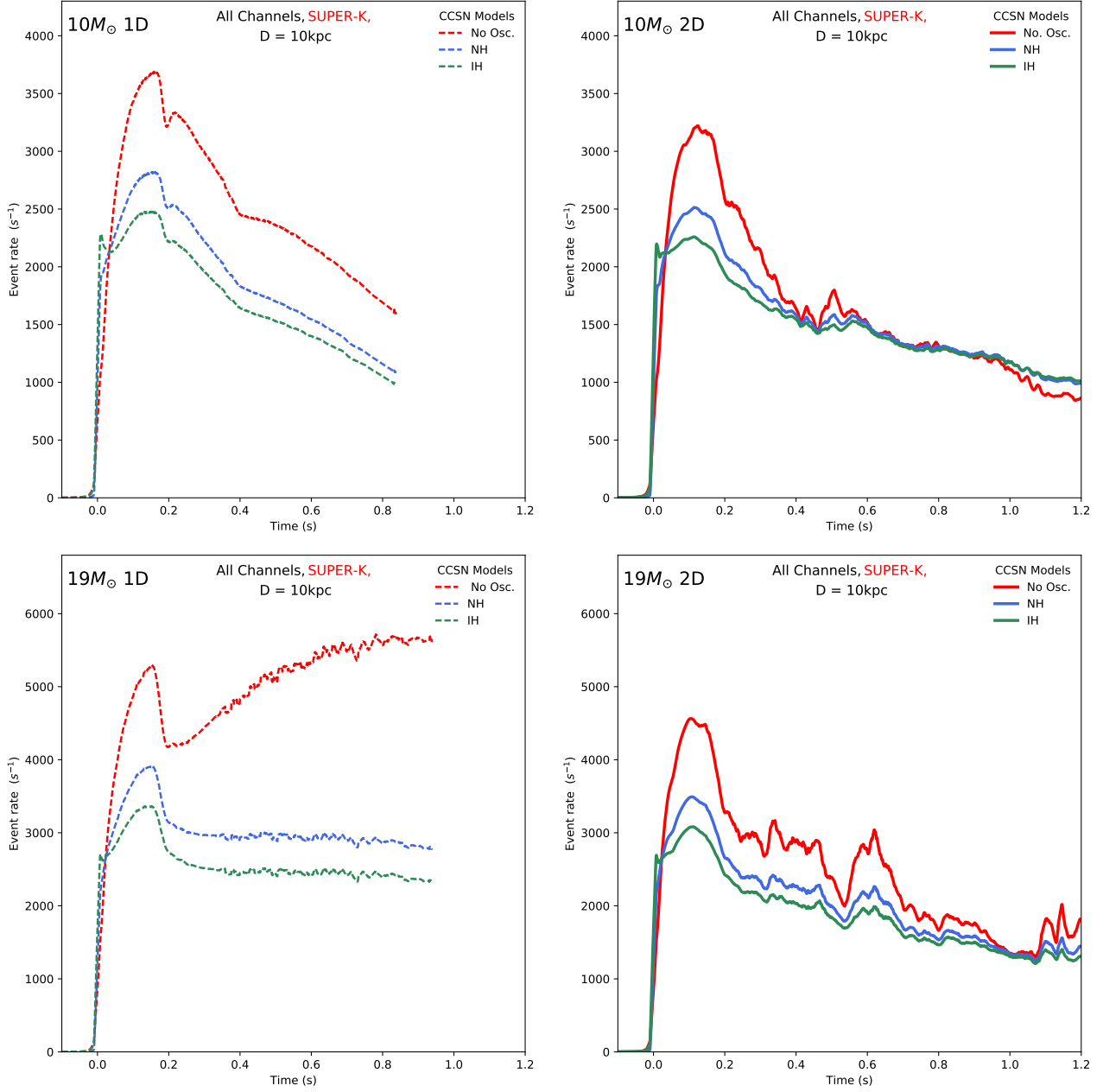


Figure 5. The total, all-channel, event rates (in units of s^{-1}) in **Super-K** at 10 kiloparsecs for all three oscillation models in 1D (left) and 2D (right) for the $10M_{\odot}$ progenitor model (top two plots) and the $19M_{\odot}$ progenitor model (bottom two plots). Note that the 1D models are all here plotted as dashed, while the 2D models are all solid. The no-oscillation case is in red, the normal-hierarchy case is in blue, and the inverted hierarchy case is in green.

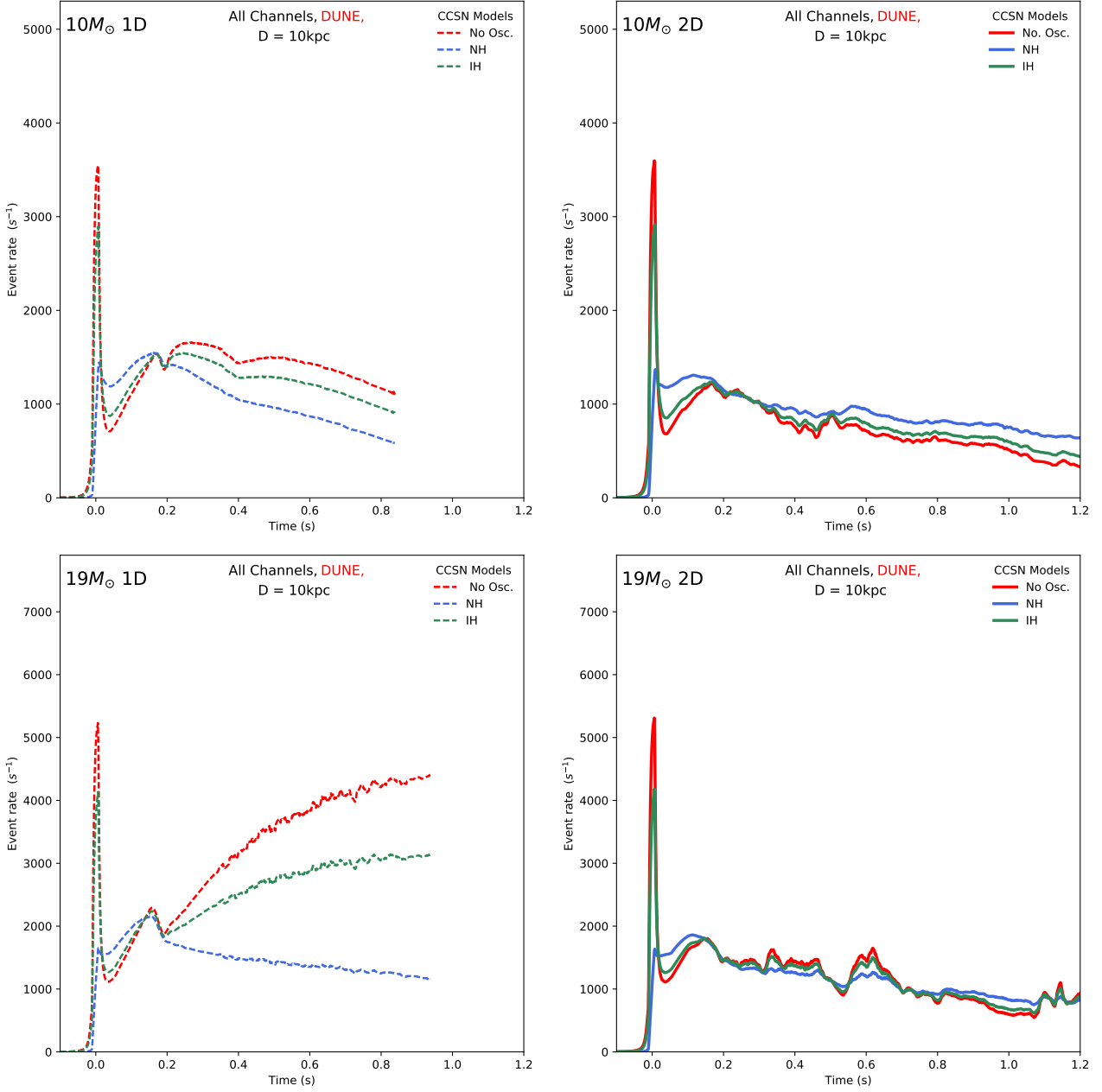


Figure 6. The total, all-channel, event rates (in units of s^{-1}) in DUNE at 10 kiloparsecs for all three oscillation models in 1D (left) and 2D (right) for the $10M_{\odot}$ progenitor model (top two plots) and the $19M_{\odot}$ progenitor model (bottom two plots). As in Figure 5, the 1D models are all plotted as dashed, while the 2D models are all solid.

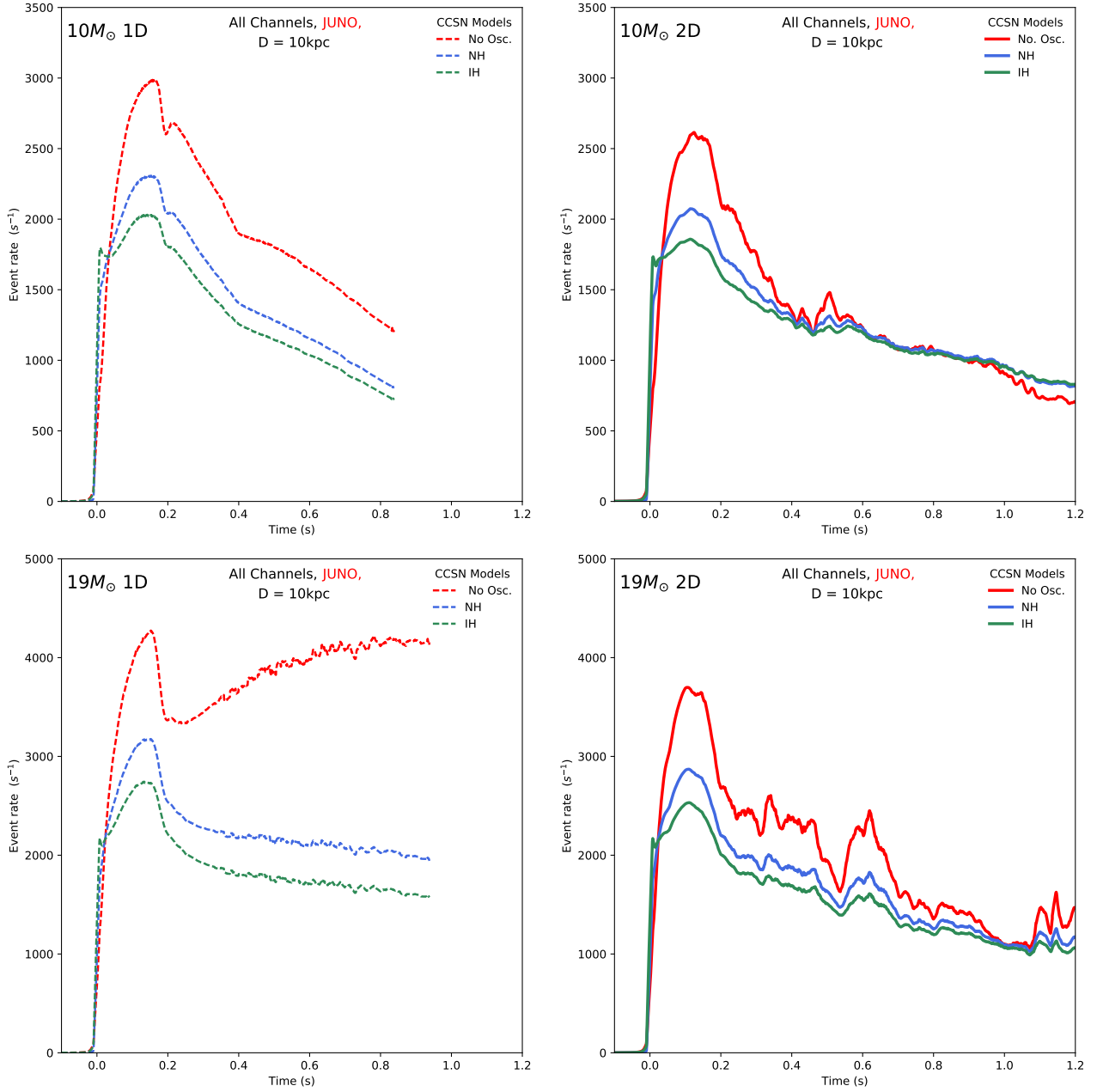


Figure 7. The total, all-channel, event rates (in units of s^{-1}) in JUNO at 10 kiloparsecs for all three oscillation models in 1D (left) and 2D (right) for the $10M_{\odot}$ progenitor model (top two plots) and the $19M_{\odot}$ progenitor model (bottom two plots). As in Figure 5, the 1D models are all plotted as dashed, while the 2D models are all solid.

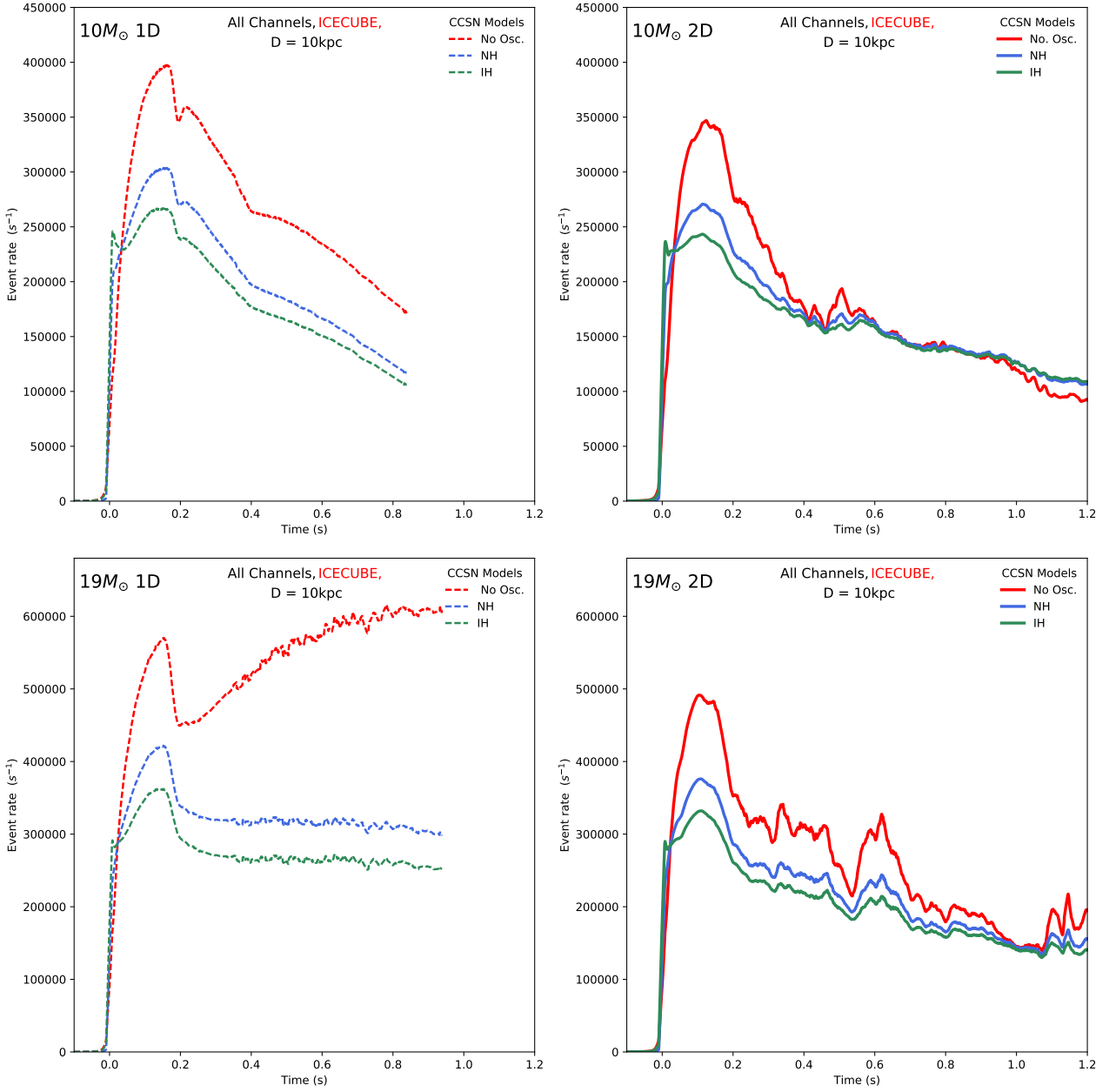


Figure 8. The total, all-channel, event rates (in units of s^{-1}) in **IceCube** at 10 kiloparsecs for all three oscillation models in 1D (left) and 2D (right) for the $10M_{\odot}$ progenitor model (top two plots) and the $19M_{\odot}$ progenitor model (bottom two plots). As in Figure 5, the 1D models are all plotted as dashed, while the 2D models are all solid.

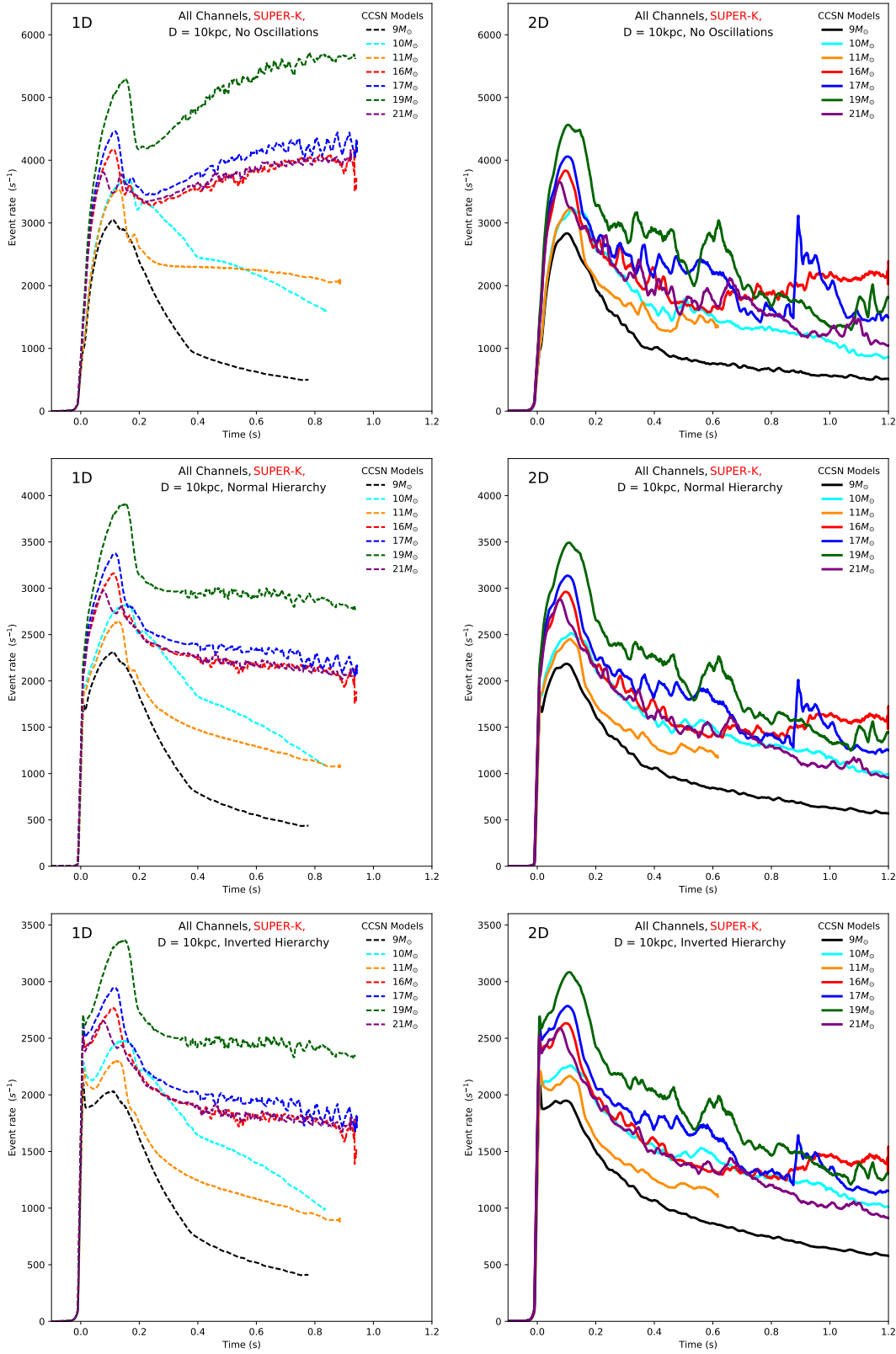


Figure 9. The total, all-channel, event rates (in units of s^{-1}) in **Super-K** at 10 kiloparsecs in the 1D (non-exploding) and 2D (exploding) calculations for all the progenitor models ($9, 10, 11, 16, 17, 19,$ and $21 M_{\odot}$) addressed in this study. The left plots are for the 1D models (in this paper, non-exploding) and the right plots are for the 2D models (exploding). The non-oscillation cases are in the top pair of figures, the normal hierarchy results are depicted in the middle pair, and the inverted hierarchy results are shown in the bottom pair (again, 1D [left], 2D [right]). As above in Figures 5 through 8, the 1D models are all plotted as dashed, while the 2D models are all solid.

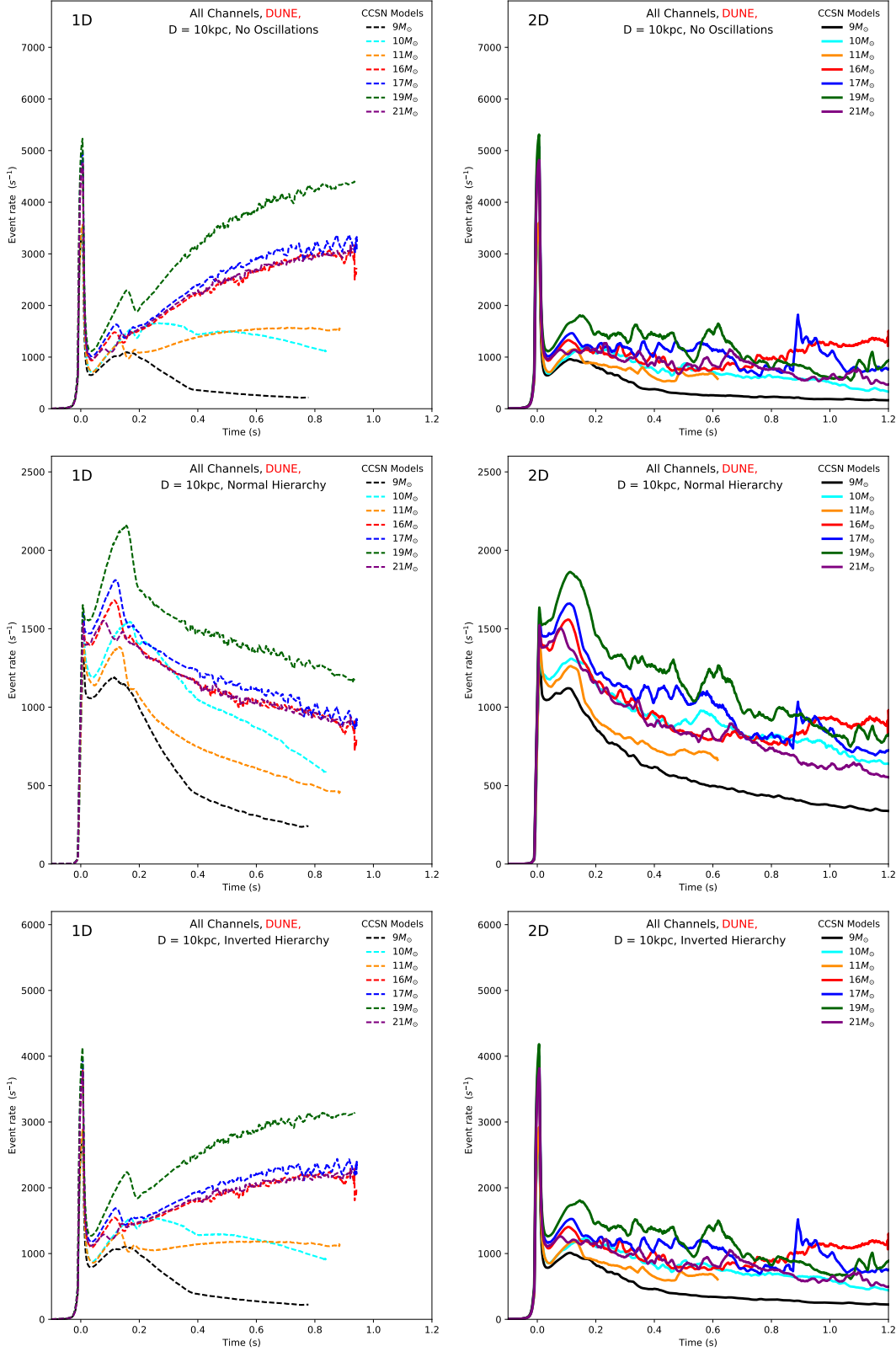


Figure 10. The same as Figure 9, but for DUNE.

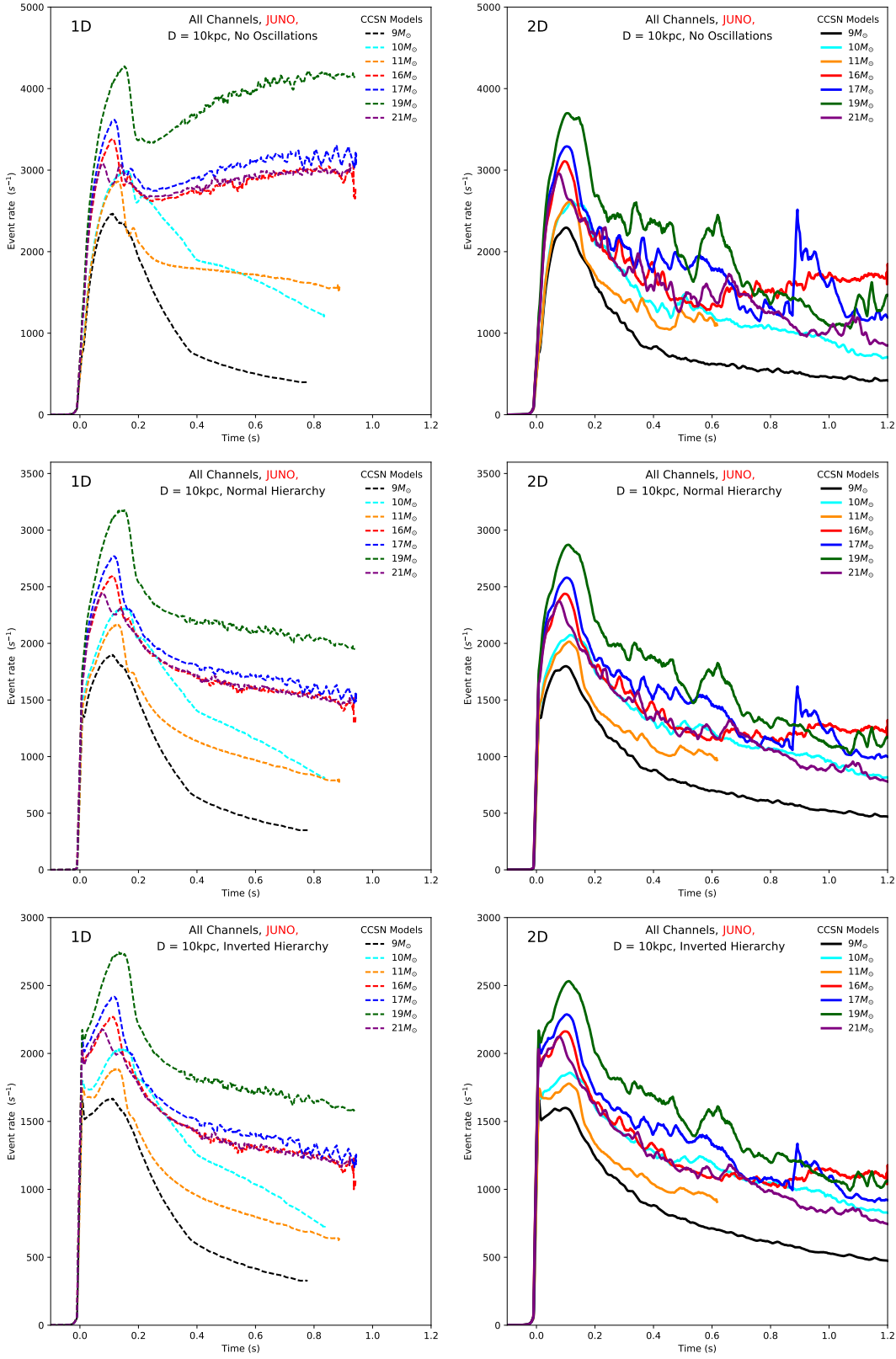


Figure 11. The same as Figure 9, but for JUNO.

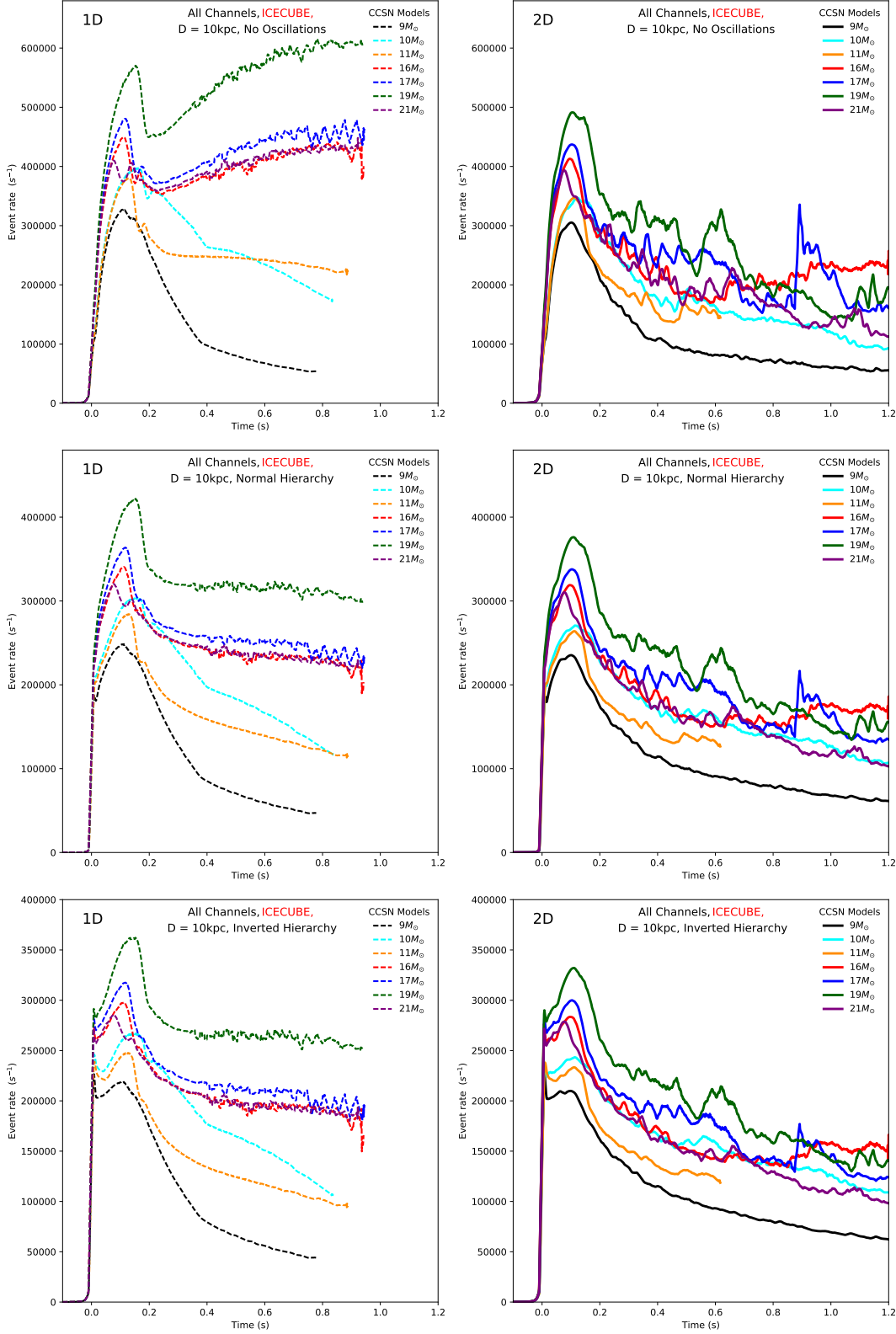


Figure 12. The same as Figure 9, but for IceCube.

This paper has been typeset from a $\text{\TeX}/\text{\LaTeX}$ file prepared by the author.